Nonlinear transport associated with spin density wave dynamics in $Ca_3Co_4O_9$

N. Murashige, F. Takei, K. Saito, and R. Okazaki
Department of Physics, Faculty of Science and Technology, Tokyo University of Science, Noda 278-8510, Japan
(Received 19 April 2017; revised manuscript received 6 June 2017; published 14 July 2017)

We have carried out the transient nonlinear transport measurements on the layered cobalt oxide $Ca_3Co_4O_9$, in which a spin density wave (SDW) transition is proposed at $T_{SDW} \simeq 30$ K. We find that, below T_{SDW}, the electrical conductivity systematically varies with both the applied current and the time, indicating a close relationship between the observed nonlinear conduction and the SDW order in this material. The time dependence of the conductivity is well analyzed by considering the dynamics of SDW which involves a low-field deformation and a sliding motion above a threshold field. We also measure the transport properties of the isovalent Sr-substituted systems to examine an impurity effect on the nonlinear response, and discuss the obtained threshold fields in terms of thermal fluctuations of the SDW order parameter.

DOI: 10.1103/PhysRevB.96.035126

I. INTRODUCTION

The quasi-two-dimensional cobalt oxide $Ca_3Co_4O_9$ provides a fascinating research playground to examine the unusual transport of strongly correlated electrons, which is characterized by the intimate coupling with its complicating structural and magnetic properties. This compound consists of two subsystems of CdI_2-type CoO_2 and rocksalt-type Ca_2CoO_3 layers, alternately stacked along the c axis [1,2]. The former is responsible for the charge transport and the latter behaves as the charge reservoir to supply holes into the conduction layer [3–6]. As is distinct from other layered systems such as the high-T_c cuprates, these subsystems have different b axis parameters (b_1 being for the rocksalt and b_2 for the CoO_2 layers). The misfit ratio is $b_1/b_2 \simeq 1.62$, thus $[Ca_2CoO_3][CoO_2]_{1.62}$ is more realistic, whereas we refer to this system as the approximate formula $Ca_3Co_4O_9$.

$Ca_3Co_4O_9$ exhibits several magnetic transitions with respect to temperature. Around room temperature, this material is paramagnetic and the cobalt ions take the low spin state. Above room temperature, the magnetic susceptibility shows an anomaly at $T = 380$ K, although the spin-state nature at higher temperature is not elucidated [7–9]. With decreasing temperature, a short-range order of spin density wave (SDW) develops below 100 K, and the long-range order appears below $T_{SDW} \simeq 30$ K [7,8]. The SDW coexists with a ferrimagnetism below $T_{FR} = 19$ K.

The unsolved issue is how such complicating magnetism relates to the transport properties. This compound shows a metallic resistivity with a large Seebeck coefficient reaching $S \simeq 130\,\mu$V/K at around room temperature [1], which is qualitatively understood with a large spin entropy flow associated with the charge (hole) hopping among the low-spin cobalt ions [10–12]. With lowering temperature, the resistivity shows a Fermi-liquid behavior with $\rho(T) = \rho_0 + AT^2$ around 120 K (Fig. 1) as is widely seen in strongly correlated electron systems, but below $T \sim 70$ K, it increases like an insulator while the Seebeck coefficient shows a metallic behavior [13]. Such a resistivity upturn may invoke the variable range hopping transport with $\rho(T) \propto \exp(T^{-\alpha})\,(0 < \alpha < 1)$ [14], but it is also claimed that the measured temperature dependence of the resistivity is much milder and that the fitting range is narrow. Limelette *et al.* have shown a large negative magnetoresistance at low temperatures, indicating a spin-dependent scattering mechanism [15]. Hsieh *et al.* have found that the conductivity is well scaled with the Seebeck coefficient for a two-dimensional metal, suggesting a reduction of the carrier density with decreasing temperature due to a pseudogap opening associated with the SDW formation [16]. Such a close relation between the resistivity upturn and the SDW order is also seen in the related layered oxide Na_xCoO_2 [17,18]. On the other hand, recent theoretical study suggests that such a resistivity increase is not necessarily related to the magnetic transitions [19], leaving the underlying origin of the transport properties unclear.

Here, we have performed the nonlinear conduction measurements on $Ca_3Co_4O_9$ single crystals to examine the electric-field response of the SDW. We measure the time dependence of the conductivity under a short current pulse at several temperatures. A clear nonlinear conduction, characterized by a systematic change in the conductivity by applied current and time, has been observed below T_{SDW}, and the time dependence of the conductivity is well understood by considering the dynamics of SDW including a low-field deformation and a high-field sliding motion. This result indicates an intimate coupling of the low-temperature transport with the SDW order in this system. Moreover, to reveal the impurity effect, the nonlinear conduction of the isovalent Sr-substituted $Ca_{3-x}Sr_xCo_4O_9$ is also measured. We discuss the thermal fluctuation effect on the SDW order to explain the obtained temperature and Sr-content dependencies of the threshold field.

II. EXPERIMENTS

The experiments were performed using $Ca_{3-x}Sr_xCo_4O_9$ single crystals ($x = 0, 0.1, 0.2$) with typical sample dimensions of $1 \times 1 \times 0.04\,\text{mm}^3$ grown by a flux method [20]. Powders of $CaCO_3$ (99.9%), $SrCO_3$ (99.9%), and Co_3O_4 (99.9%) were mixed in a stoichiometric ratio and calcined two times in air at 1173 K for 24 h with intermediate grindings. Then KCl (99.999%) and K_2CO_3 (99.999%) powders mixed with a molar ratio of 4:1 was added with the calcined powder as a flux. The concentration of $Ca_{3-x}Sr_xCo_4O_9$ was set to be 1.5% in molar ratio. The mixture was put in an alumina crucible and heated up to 1123 K in air with a heating rate of 200 K/h. After

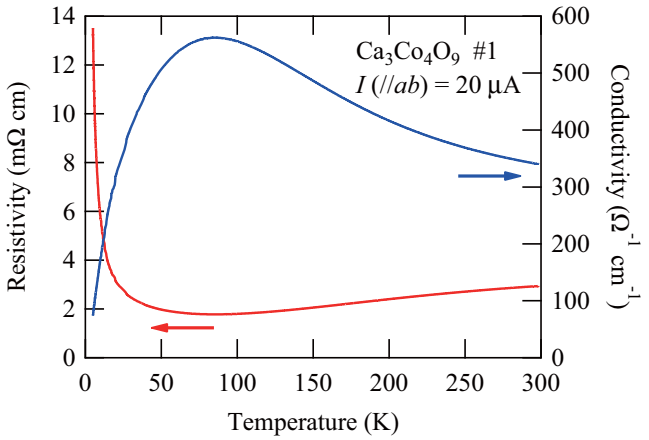

FIG. 1. Temperature variations of the in-plane resistivity (left axis) and the conductivity (right axis) of $Ca_3Co_4O_9$ single crystal (sample No. 1 with low contact resistance) measured with a low excitation current of $I = 20\,\mu$A.

keeping 1123 K for 1 h, it was slowly cooled down with a rate of 1 K/h, and at 1023 K, the power of the furnace was switched off. As-grown samples were rinsed in distilled water to remove the flux.

The resistivity was measured using a standard four-probe method along the in-plane direction. The transient measurement was performed using a Keithley 6221 current source and a 2182A nanovoltmeter, which were synchronously operated in a built-in pulse mode. The pulse width of the excitation current was set to be 160 μs. The pulse interval was set to be 100 ms, which is sufficiently long to reduce the Joule heating. The time dependence of the sample voltage was measured by changing the delay time from the leading edge of the current pulse for the voltage measurement, as is schematically depicted in the inset of Fig. 2(f). Owing to the limitation of the equipment, the minimum delay time is about 20 μs.

The electrodes were made by two kinds of silver paints to check the effect of the contact resistance. Except for $Ca_3Co_4O_9$ sample No. 2, we used Dupont 6838, which was cured above 473 K for 2 h, and achieved a relatively low contact resistance of $R_{\rm contact} \sim 10\,\Omega$ at low temperature of $T = 5$ K. On the other hand, for $Ca_3Co_4O_9$ sample No. 2, we used Dupont 4922 cured at room temperature. Compared to the former case, the contact resistance was high ($R_{\rm contact} \sim 100\,\Omega$ at $T = 5$ K). The effect of the contact resistance on the nonlinear conduction will be discussed later.

III. RESULTS AND DISCUSSION

Figure 1 shows the temperature dependencies of the resistivity ρ and the conductivity $\sigma = \rho^{-1}$ of $Ca_3Co_4O_9$ single crystal (sample No. 1) measured with a low excitation current of $I = 20\,\mu$A. As is seen in the previous studies [1], the resistivity shows a metallic temperature variation above 100 K but displays an insulating behavior at low temperatures. Figures 2(a)–2(f) depict the time variations of the conductivity of $Ca_3Co_4O_9$ single crystal (sample No. 1) measured at several temperatures in the insulating regime. At $T = 5$ K [Fig. 2(a)], the conductivity increases with increasing time and applied current, indicating a presence of nonlinear conduction in this system. The nonlinearity becomes small rapidly with increasing temperature, and it completely disappears at $T =$ 50 K as is seen in Fig. 2(f).

Here, we first note that the observed change in the conductivity does not stem from the Joule heating under the large current, which often appears in the nonlinear conduction measurements [21]. To check this extrinsic effect, we estimate the maximum temperature increase $\Delta T_{\rm max}$ by assuming that all the thermal energy produced by the Joule heating is consumed for the increase of the sample temperature. In the present study, the sample resistance (<1 Ω) is much smaller than the contact resistance $R_{\rm contact} \sim 10\,\Omega$, hence the contact resistance determines the Joule heating power. We then calculate $\Delta T_{\rm max}$ as $\Delta T_{\rm max} = R_{\rm contact} I^2 \Delta t / CV$, where I is the applied current, Δt the pulse width, C the heat capacity at $T = 5$ K [13], and V the sample volume, and obtain $\Delta T_{\rm max} \sim 0.1$ K for $I =$ 10 mA and $T = 5$ K. Since $d\sigma/dT \sim 20\,\Omega^{-1}{\rm cm}^{-1}{\rm K}^{-1}$ around $T = 5$ K, as is seen in Fig. 1, $\Delta T_{\rm max} \sim 0.1$ K corresponds to the conductivity change of $2\,\Omega^{-1}{\rm cm}^{-1}$. This maximum estimation is much smaller than the observed conductivity change as shown in Fig. 2(a), indicating an intrinsic nonlinearity in this

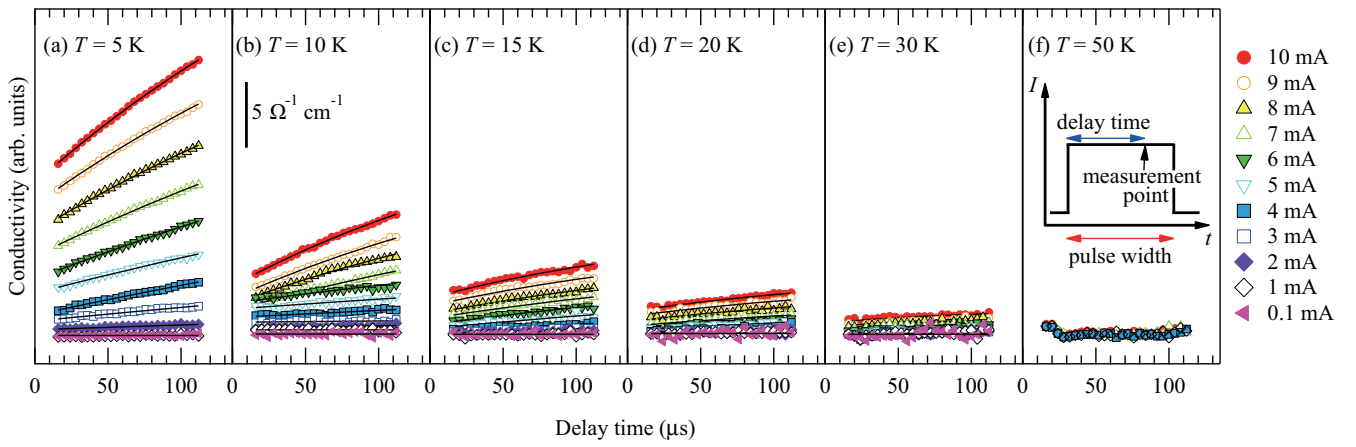

FIG. 2. (a)–(g) Time variations of the conductivity of $Ca_3Co_4O_9$ single crystal (sample No. 1 with low contact resistance) measured at several temperatures. The scale bar shown in (b) is common to all the data in (a)–(f), and the data are not shifted for each panel. The solid curves show the fitting results. The inset depicts a schematic curve of the applied current pulse.

system. We also examine the Joule heating effect by using sample No. 2 with high contact resistance, which will be discussed later.

Since the nonlinear conduction becomes negligibly small above the SDW transition temperature $T_{SDW} \sim 30$ K, we then analyze the present data by considering the dynamics of density wave. In contrast to a charge density wave (CDW), the charge density is spatially constant in an SDW. However, an SDW can be regarded as a composition of two out-of-phase CDW's formed by spin-up and spin-down electrons. Near an impurity site, the SDW will be pinned by inducing a distortion of the total electron density because the up- and down-spin components of the charge density deform differently. This is basically reduced to the coupling of the impurities to the second-order harmonic CDW that coexists with the SDW [22,23]. A similar electric field response to that of CDW is therefore expected in an SDW system and has experimentally observed [24].

Now the classical equation of motion of a density wave under electric field E is expressed as

$$\frac{d^2x}{dt^2} = -\frac{1}{\tau_s}\frac{dx}{dt} - \frac{\omega_0^2}{2k_F}\sin 2k_F x + \frac{qE}{m^*}, \tag{1}$$

where x is the displacement, τ_s a relaxation time, ω_0 a pinning frequency, k_F a Fermi wave number, q a charge, and m^* an effective mass for the density wave [24,25]. Under strong electric field, the density wave exhibits a collective sliding motion as is schematically depicted in Fig. 3(a). This motion carries an additional electrical current and increases the conductivity. In this case, the electric potential is much larger than the pinning potential. Then the restoring term may be neglected, and the equation is reduced to

$$\frac{dv}{dt} = -\frac{v}{\tau_s} + \frac{qE}{m^*}, \tag{2}$$

where $v = dx/dt$ [26]. This viscous-resistance-type equation is simply solved as

$$v(t) = \frac{q\tau_s E}{m^*}\left[1 - \exp\left(-\frac{t}{\tau_s}\right)\right]. \tag{3}$$

Thus the conductivity carried by the sliding motion of density wave σ_s is given as

$$\sigma_s(t) = \frac{n_s q v}{E} = A_s\left[1 - \exp\left(-\frac{t}{\tau_s}\right)\right], \tag{4}$$

where $A_s = n_s q^2 \tau_s / m^*$ and n_s is a carrier density participating the sliding motion of density wave. The time dependence of the conductivity $\sigma_s(t)$ is schematically shown by the red curve in Fig. 3(c). The total conductivity is then given as $\sigma_s + \sigma_0$, where σ_0 is an offset term, and the fitting well reproduces the experimental results as shown by the solid curves in Figs. 2(a)–2(f). The obtained fitting parameters will be discussed later.

We also examine the nonlinear conduction in $Ca_3Co_4O_9$ sample No. 2, in which the contact resistance is 10 times larger than that in sample No. 1. Figure 4 shows the time variations of the conductivity of $Ca_3Co_4O_9$ sample No. 2 measured at $T = 5$ K. In contrast to the results of sample No. 1 shown in Figs. 2(a)–2(f), the conductivity first decreases with increasing

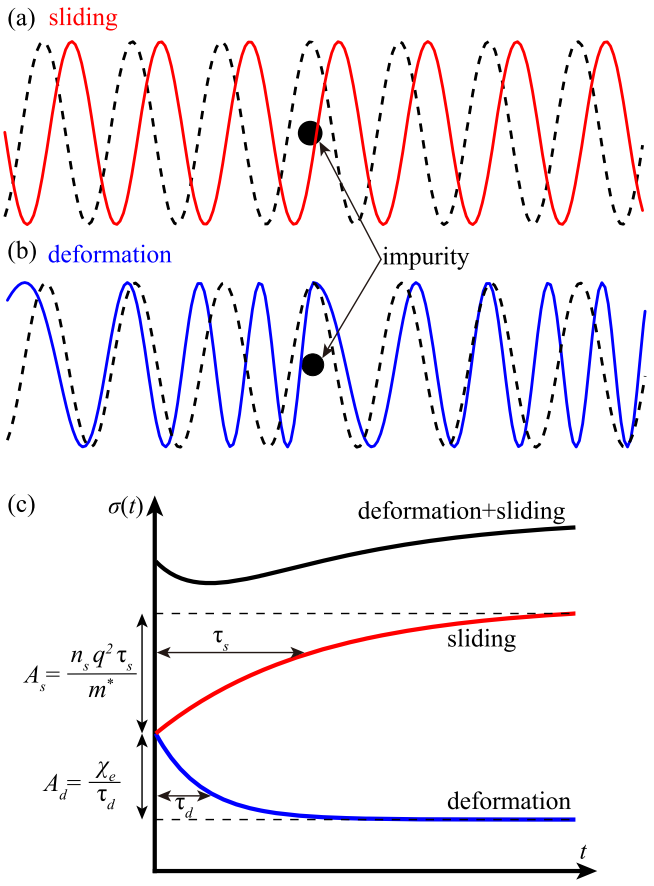

FIG. 3. Schematic pictures of (a) sliding motion and (b) deformation of spin density wave (SDW) around an impurity expressed as the solid circle. The dashed and solid curves show the SDW without and with electric field, respectively. (c) Schematic time variations of the conductivity. The red and blue curves are conductivities from sliding motion and deformation of SDW, respectively, and the black solid curve represents the total conductivity.

time in the short time range below about 30 μs. This behavior is opposite to the heating effect since the conductivity should increase with heating at this temperature range. It then turns to increase with time at the high current range like the sliding motion as is discussed before. To examine the heating effect in this range, we compare the conductivity change by currents. At the delay time of 60 μs, the conductivity changes between 1 mA and 10 mA are 17 Ω^{-1} cm^{-1} for sample No. 1 [Fig. 2(a)] and 18 Ω^{-1} cm^{-1} for sample No. 2 (Fig. 4), which are almost the same. If the heating effect is dominant, the conductivity in sample No. 2 should largely change due to the 10-times difference in the contact resistance. This result again indicates a negligible heating effect in the present study.

To explain the result of sample No. 2, we now consider the field-induced deformation of SDW in addition to the sliding motion. As is schematically depicted in Fig. 3(b), at low applied fields, a density wave is pinned by impurities and is deformed [26]. Here the resulting spatial charge modulation produces a time-dependent electric polarization $P(t)$. In density-wave materials, the Debye description is a first approximation for the dielectric relaxation process [27,28],

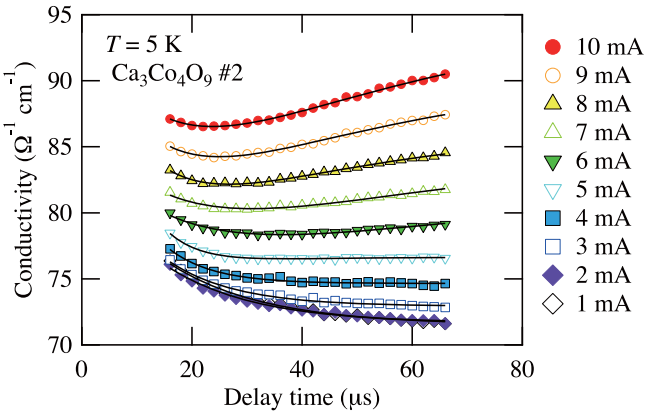

FIG. 4. Time variations of the conductivity of $Ca_3Co_4O_9$ single crystal (sample No. 2 with high contact resistance) measured at $T = 5$ K. The solid curves show the fitting results. For details see text.

hence we use

$$\frac{dP(t)}{dt} = -\frac{P(t)}{\tau_d} + \frac{\chi_e E}{\tau_d}, \tag{5}$$

where τ_d is a relaxation time for the deformation process and χ_e is an electric susceptibility. This is solved as $P(t) = \chi_e E[1 - \exp(-t/\tau_d)]$. We thus obtain the polarization current $j_P = dP/dt$ and the deformation-induced conductivity $\sigma_d = j_P/E$ expressed as

$$\sigma_d(t) = \frac{\chi_e}{\tau} \exp\left(-\frac{t}{\tau}\right), \tag{6}$$

as is schematically drawn by the blue curve in Fig. 3(c).

Therefore the total conductivity is given as $\sigma(t) = \sigma_s(t) + \sigma_d(t) + \sigma_0$. The time dependence of the total conductivity is schematically displayed by the black curve in Fig. 3(c), and the fitting results for sample No. 2 are shown by solid curves in Fig. 4, which also well reproduce the experimental data. Note that the deformation-induced conductivity has not been monitored in sample No. 1, as is seen in Figs. 2(a)–2(f). We consider that, since the polarization current is induced by the electric dipoles pinned at the interface between the sample and the electrode, it will be sensitive to the amount of the impurities at the interface, hence the deformation-induced conductivity has been observed only in sample No. 2 with high contact resistance.

In Figs. 5(a)–5(d), we summarize the fitting parameters obtained at $T = 5$ K. Figures 5(a) and 5(c) display the electric field dependencies of the scattering rate τ_s^{-1} for sample No. 1 and sample No. 2 (left axis), respectively. Here the electric field is obtained by averaging at each applied current. For both samples, the scattering rate becomes large with increasing electric field since the velocity of the sliding motion increases in the high fields. Figures 5(b) and 5(d) show A_s/τ_s as a function of the electric field for sample No. 1 and sample No. 2 (left axis), respectively. Since $A_s = n_s q^2 \tau_s/m^*$, A_s/τ_s is proportional to the carrier density which participates the sliding motion of SDW. At low fields, A_s/τ_s is almost zero due to the pinning of SDW by impurities. Above the threshold field $E_{\rm th}$, A_s/τ_s increases with increasing electric field since the number of depinned SDW increases in the high-field range.

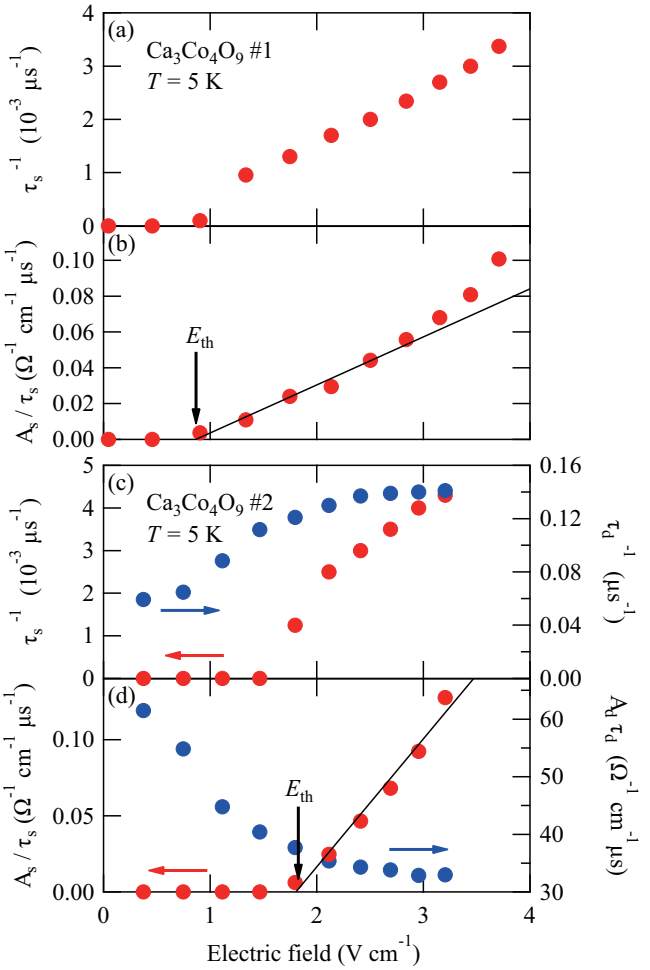

FIG. 5. Electric field dependence of (a) the scattering rate for the sliding motion τ_s^{-1} and (b) A_s/τ_s ($\propto n_s$) for sample No. 1 at $T = 5$ K. The solid arrow represents the threshold field $E_{\rm th}$. (c) Electric field dependence of the scattering rate for the sliding motion (red circles, left axis) and the deformation process (blue circles, right axis) for sample No. 2 measured at $T = 5$ K. (d) Electric field dependence of A_s/τ_s ($\propto n_s$) (red circles, left axis) and the electric susceptibility $A_d\tau_d$ ($= \chi_e$) (blue circles, right axis) for sample No. 2 measured at $T = 5$ K.

We also stress that the electric field dependencies of τ_s and A_s/τ_s do not differ significantly between samples No. 1 and No. 2, because the conductivity changes are almost the same as discussed before.

We plot the electric field variations of τ_d^{-1} and $A_d\tau_d$ obtained for sample No. 2 at $T = 5$ K in the right axes of Figs. 5(c) and 5(d), respectively. The relaxation time for the deformation decreases with increasing electric field as is the case in the sliding motion. The electric susceptibility $A_d\tau_d$ ($= \chi_e$) gradually decreases with increasing electric field and shows a weak electric field dependence above the threshold field. This indicates that the polarization becomes small with increasing electric field owing to the depinning of the SDW. The background signal of $A_d\tau_d$ above the threshold field may originate from an extrinsic origin such as an unwanted capacitance component at the electrode due to the high contact resistance of sample No. 2.

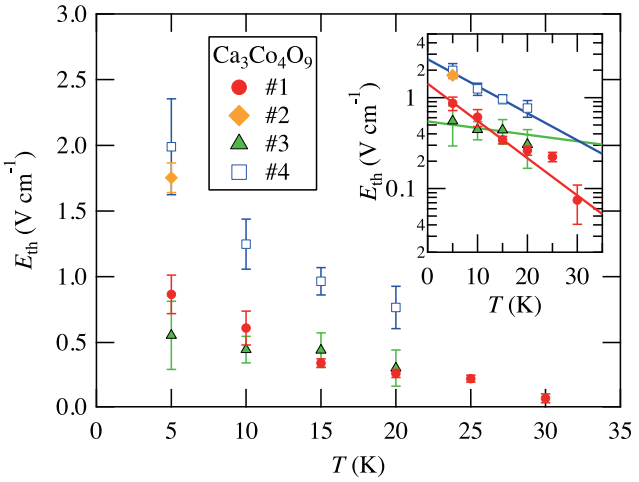

FIG. 6. Temperature dependence of the threshold field E_{th} of four samples of $Ca_3Co_4O_9$. The inset shows E_{th} vs T in the log-linear scale. The solid lines represent the fitting results using $\ln E_{th}(T) = \ln E_{th}(0) - T/T_0$.

The temperature dependence of the threshold field E_{th} measured for several samples is plotted in Fig. 6. The threshold field decreases with increasing temperature, indicating a thermal fluctuation effect on the SDW order. The threshold field under thermal fluctuations is theoretically given as

$$E_{th}(T)/E_{th}(0) = \exp(-T/T_0), \tag{7}$$

for a low-temperature range of $T \lesssim \frac{1}{2}T_{SDW}$, where $T_0 \sim \eta^2(k_F\xi)T_F$, $\eta = v_F^c/v_F^{ab} < 1$ is the anisotropy of the Fermi velocity, ξ the coherence length of the SDW, T_F the Fermi temperature [29]. We then plot E_{th} vs T data in the log-linear scale in the inset of Fig. 6. The data are fitted for a low-temperature range $T \leqslant 15$ K, and as shown by the fitting lines, $E_{th}(T)$ well obey this behavior, suggesting the dominant thermal fluctuation effect.

Although $E_{th}(T)$ in the parent compounds shows qualitatively similar temperature variations, the resultant fitting parameters, $E_{th}(0)$ and T_0, are strongly sample dependent as is obviously seen in Fig. 6, indicating that the uncontrollable impurities such as the oxygen defects may affect $E_{th}(T)$. Thus we have measured the nonlinear conduction in the isovalent compounds $Ca_{3-x}Sr_xCo_4O_9$ ($x = 0.1, 0.2$) to clarify the impurity effect on the threshold field. Similar nonlinear conduction has also been observed in the Sr-substituted systems, and the obtained threshold fields are presented in Fig. 7(a) as a function of temperature. Since the μSR study has revealed that the Sr substitution does not affect the SDW transition temperature [7], we fit the data using Eq. (7) for the temperature range of $T \leqslant 15$ K, as is depicted by the solid lines.

Figure 7(b) displays $E_{th}(0)$ as a function of T_0^{-1} obtained for several samples of $Ca_{3-x}Sr_xCo_4O_9$, roughly showing a positive correlation between $E_{th}(0)$ and T_0^{-1} in this cobaltite. Here, $E_{th}(0)$ is sensitive to the amount of impurity, as is theoretically given by $E_{th}(0) \propto c$ for the strong pinning limit, where c is the impurity concentration [29], and $T_0^{-1} \propto \xi^{-1} = \xi_0^{-1} + \xi_{imp}^{-1}$, where $\xi_0 \simeq \hbar v_F/\pi k_B T_{SDW}$ and ξ_{imp} is a mean free math determined by the amount of impurities [25]. Since

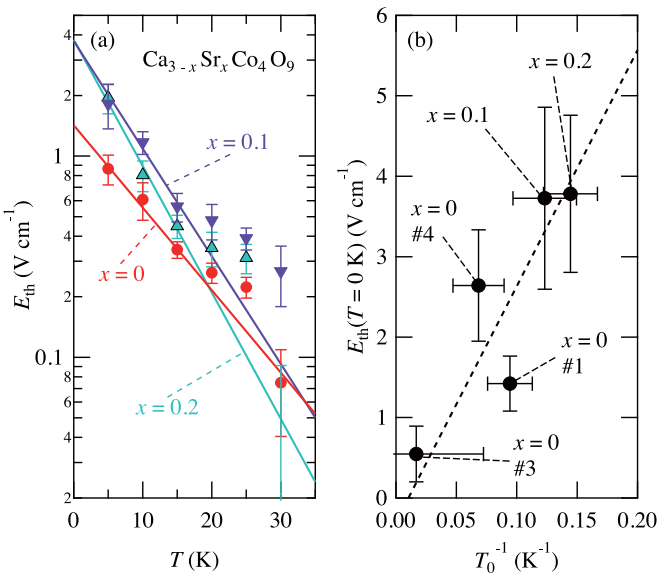

FIG. 7. (a) Temperature dependence of the threshold field of $Ca_{3-x}Sr_xCo_4O_9$ ($x = 0, 0.1, 0.2$) shown in the linear-log scale. The solid lines represent the fitting results. (b) Relation between $E_{th}(0)$ and T_0^{-1} for several samples of $Ca_{3-x}Sr_xCo_4O_9$. The dashed line represents a linear T_0^{-1} dependence of $E_{th}(0)$.

ξ_{imp}^{-1} represents an impurity concentration per unit length, a relation of $E_{th}(0) \propto \xi_{imp}^{-1} \propto T_0^{-1} + A$ (A being a constant) is expected, and the experimental data roughly show this linear T_0^{-1} dependence of $E_{th}(0)$ as depicted by the dashed line in Fig. 7(b). To further examine the impurity effect, we compare two characteristic lengths, ξ_0 and ξ_{imp}. Using the carrier concentration $n \simeq 6 \times 10^{21}$ cm^{-3} [30] and the effective mass $m^* \simeq 13m_0$ [31], ξ_0 is calculated as $\xi_0 \simeq 4$ nm. On the other hand, ξ_{imp} is estimated as $\xi_{imp} \simeq 4$ nm for the $x = 0.1$ sample [32], comparable to ξ_0, indicating that the impurities certainly affect the temperature dependence of the threshold field in this system. To examine more precisely, the impurity effect using both nonmagnetic and magnetic ions should be clarified as a future study.

The present study including the Sr substitution effect certainly shows an intimate relationship between the low-temperature transport and the SDW order. Interestingly, the resistivity upturn reminiscent of the present system has also been observed in other misfit cobaltites with different block-layer structures [33]. Thus nonlinear conduction should also be examined in such systems as a future study to clarify the ubiquitous nature among the layered cobalt oxides. Moreover, since the low-temperature conductivity in $Ca_3Co_4O_9$ is suggested to be scaled to the Seebeck coefficient [16], the electric field effect on other transport properties including the Seebeck coefficient and the thermal conductivity is also crucial to elucidate the inherent conduction mechanism far from equilibrium [34,35].

IV. SUMMARY

We have studied the nonlinear conduction phenomena in the layered cobalt oxide $Ca_3Co_4O_9$ and the Sr-substituted systems. Below the SDW transition temperature, the electrical conductivity largely varies with both the applied current and

the time, indicating that the observed nonlinear conduction is caused by a dynamics of SDW. We analyze the time dependence of the conductivity in terms of the low-field deformation and the high-field sliding motion of SDW, and find that the temperature and Sr-content variations of the threshold fields are qualitatively understood within a thermal fluctuation effect on the SDW.

ACKNOWLEDGMENTS

We thank K. Kanai, Y. Maeno, and S. Yonezawa for discussion and R. Adachi and H. Koike for experimental support. This work was supported by a Grant-in-Aid for Challenging Exploratory Research (Grant No. 26610099) from JSPS, and start-up research funding for young scientists from Tokyo University of Science.

[1] A. C. Masset, C. Michel, A. Maignan, M. Hervieu, O. Toulemonde, F. Studer, B. Raveau, and J. Hejtmanek, Phys. Rev. B **62**, 166 (2000).

[2] Y. Miyazaki, M. Onoda, T. Oku, M. Kikuchi, Y. Ishii, Y. Ono, Y. Morii, and T. Kajitani, J. Phys. Soc. Jpn. **71**, 491 (2002).

[3] T. Mizokawa, L. H. Tjeng, H.-J. Lin, C. T. Chen, R. Kitawaki, I. Terasaki, S. Lambert, and C. Michel, Phys. Rev. B **71**, 193107 (2005).

[4] G. Yang, Q. Ramasse, and R. F. Klie, Phys. Rev. B **78**, 153109 (2008).

[5] R. F. Klie, Q. Qiao, T. Paulauskas, A. Gulec, A. Rebola, S. Öğüt, M. P. Prange, J. C. Idrobo, S. T. Pantelides, S. Kolesnik, B. Dabrowski, M. Ozdemir, C. Boyraz, D. Mazumdar, and A. Gupta, Phys. Rev. Lett. **108**, 196601 (2012).

[6] K. Tanabe, R. Okazaki, H. Taniguchi, and I. Terasaki, J. Phys.: Condens. Matter **28**, 085601 (2016).

[7] J. Sugiyama, H. Itahara, T. Tani, J. H. Brewer, and E. J. Ansaldo, Phys. Rev. B **66**, 134413 (2002).

[8] J. Sugiyama, J. H. Brewer, E. J. Ansaldo, H. Itahara, K. Dohmae, Y. Seno, C. Xia, and T. Tani, Phys. Rev. B **68**, 134423 (2003).

[9] Y. Wakisaka, S. Hirata, T. Mizokawa, Y. Suzuki, Y. Miyazaki, and T. Kajitani, Phys. Rev. B **78**, 235107 (2008).

[10] W. Koshibae, K. Tsutsui, and S. Maekawa, Phys. Rev. B **62**, 6869 (2000).

[11] W. Koshibae and S. Maekawa, Phys. Rev. Lett. **87**, 236603 (2001).

[12] J. Hejtmánek, Z. Jirák, and J. Šebek, Phys. Rev. B **92**, 125106 (2015).

[13] P. Limelette, V. Hardy, P. Auban-Senzier, D. Jérome, D. Flahaut, S. Hébert, R. Frésard, C. Simon, J. Noudem, and A. Maignan, Phys. Rev. B **71**, 233108 (2005).

[14] A. Bhaskar, Z.-R. Lin, and C.-J. Liu, J. Mater. Sci. **49**, 1359 (2014).

[15] P. Limelette, J. C. Soret, H. Muguerra, and D. Grebille, Phys. Rev. B **77**, 245123 (2008).

[16] Y.-C. Hsieh, R. Okazaki, H. Taniguchi, and I. Terasaki, J. Phys. Soc. Jpn. **83**, 054710 (2014).

[17] J. Sugiyama, J. H. Brewer, E. J. Ansaldo, H. Itahara, T. Tani, M. Mikami, Y. Mori, T. Sasaki, S. Hébert, and A. Maignan, Phys. Rev. Lett. **92**, 017602 (2004).

[18] M. Lee, L. Viciu, L. Li, Y. Wang, M. L. Foo, S. Watauchi, R. A. Pascal, R. J. Cava, and N. P. Ong, Nat. Mater. **5**, 537 (2006).

[19] S. Lemal, J. Varignon, D. I. Bilc, and P. Ghosez, Phys. Rev. B **95**, 075205 (2017).

[20] Y. Ikeda, K. Saito, and R. Okazaki, J. Appl. Phys. **119**, 225105 (2016).

[21] R. Okazaki, Y. Nishina, Y. Yasui, F. Nakamura, T. Suzuki, and I. Terasaki, J. Phys. Soc. Jpn. **82**, 103702 (2013); and references therein.

[22] P. F. Tua and J. Ruvalds, Phys. Rev. B **32**, 4660 (1985).

[23] S. Tomić, J. R. Cooper, D. Jérome, and K. Bechgaard, Phys. Rev. Lett. **62**, 462 (1989).

[24] P. Monceau, Adv. Phys. **61**, 325 (2012).

[25] G. Grüner, Rev. Mod. Phys. **60**, 1129 (1988); **66**, 1 (1994).

[26] M. Sasaki, G. Houzaki, M. Koyano, and M. Inoue, J. Phys. Chem. Solids **57**, 281 (1996).

[27] R. J. Cava, R. M. Fleming, P. Littlewood, E. A. Rietman, L. F. Schneemeyer, and R. G. Dunn, Phys. Rev. B **30**, 3228 (1984).

[28] G. Mihály, Y. Kim, and G. Grüner, Phys. Rev. Lett. **66**, 2806 (1991).

[29] K. Maki, Phys. Rev. B **33**, 2852 (1986).

[30] M. Schrade, T. Norby, and T. G. Finstad, J. Appl. Phys. **117**, 205103 (2015).

[31] Y. Wang, Y. Sui, P. Ren, L. Wang, X. Wang, W. Su, and H. Fan, Chem. Mater. **22**, 1155 (2010).

[32] The unit cell of the rocksalt-type Ca_2CoO_3 layer contains four Ca ions and the lattice constant is $a \sim b_1 \sim 0.5$ nm, leading to a rough estimation of the Sr-Sr distance of $0.5 \times 30/4 \simeq 4$ nm for $x = 0.1$ sample.

[33] R. Wei, X. Tang, L. Hu, X. Zhu, J. Yang, W. Song, J. Dai, X. Zhu, and Y. Sun, J. Alloys Compd. **694**, 333 (2017).

[34] J. P. Stokes, A. N. Bloch, A. Janossy, and G. Grüner, Phys. Rev. Lett. **52**, 372 (1984).

[35] G. Kriza, A. Jánossy, and L. Forró, Phys. Rev. B **41**, 5451 (1990).